

Truncated kernel windowed Fourier projection: a fast algorithm for the 3D free-space wave equation

Nour G. Al Hassanieh^a, Alex H. Barnett^a, Leslie Greengard^{a,b}

^aCenter for Computational Mathematics, Flatiron Institute, Simons Foundation, New York, New York 10010

^bCourant Institute of Mathematical Sciences, New York University, New York, New York 10012

Abstract

We present a spectrally accurate fast algorithm for evaluating the solution to the scalar wave equation in free space driven by a large collection of point sources in a bounded domain. With M sources temporally discretized by N_t time steps of size Δt , a naive potential evaluation at M targets on the same time grid requires $\mathcal{O}(M^2 N_t)$ work. Our scheme requires $\mathcal{O}((M + N^3 \log N) N_t)$ work, where N scales as $\mathcal{O}(1/\Delta t)$, i.e., the maximum signal frequency. This is achieved by using the recently-proposed windowed Fourier projection (WFP) method to split the potential into a local part, evaluated directly, plus a smooth history part approximated by an N^3 -point equispaced discretization of the Fourier transform, where each Fourier coefficient obeys a simple recursion relation. The growing oscillations in the spectral representation (which would be present with a naive use of the Fourier transform) are controlled by spatially truncating the hyperbolic Green's function itself. Thus, the method avoids the need for absorbing boundary conditions. We demonstrate the performance of our algorithm with up to a million sources and targets at 6-digit accuracy. We believe it can serve as a key component in addressing time-domain wave equation scattering problems.

Keywords: wave equation, free-space, hyperbolic potentials, high-order, truncated kernel, Fourier methods

1. Introduction

We present a fast algorithm to compute free-space hyperbolic potentials in 3D to high accuracy without the need for artificial absorbing boundary conditions. Such potentials are space-time convolutions of the free-space retarded Green's function with a given source distribution; the latter could be a singular density supported on a boundary (a layer potential) [1–3], a smooth density supported in a bounded domain (a volume potential), or a set of point-like scatterers. For our present purposes, we assume that the source distribution has already been spatially discretized as a large collection of points. Other aspects of potential theory, including integral representations, quadrature design, and the application of our fast algorithm to time-marching the integral equation solution will be considered at a later date. However, there are many advantages to using integral equation methods [2, 4–9]. In particular, they do not require absorbing boundary conditions to avoid spurious reflections from a finite computational domain, and (in the homogeneous case), they discretize the boundary alone, without the need for complicated mesh generation. The rapid evaluation of such potentials accelerates time-domain integral equation-based schemes for the solution of wave scattering problems. The latter are essential in many scientific and engineering applications such as acoustics [10, 11] and, generalizing to vectorial cases, electromagnetic/optical scattering [4, 5, 9, 12, 13] and seismic propagation [14]. The time-domain approach to such problems is especially useful when faced with wide-band signals and/or nonlinear materials.

In this paper, we consider the solution of the free-space wave equation

$$\partial_t^2 u(\mathbf{x}, t) - \Delta u(\mathbf{x}, t) = f(\mathbf{x}, t), \quad \mathbf{x} \in \mathbb{R}^3, \quad t \in (0, T], \quad (1a)$$

$$u(\mathbf{x}, 0) = \partial_t u(\mathbf{x}, 0) = 0, \quad \mathbf{x} \in \mathbb{R}^3. \quad (1b)$$

Email addresses: nal Hassanieh@flatironinstitute.org (Nour G. Al Hassanieh), abarnett@flatironinstitute.org (Alex H. Barnett), lgreengard@flatironinstitute.org (Leslie Greengard)

The forcing function f will be assumed to be a sum of M point sources located at \mathbf{y}_j , $j = 1, \dots, M$, with smooth time signatures $\sigma_j(t)$, such that $\sigma_j(t) = 0$ for $t \leq 0$:

$$f(\mathbf{x}, t) = \sum_{j=1}^M \delta(\mathbf{x} - \mathbf{y}_j) \sigma_j(t), \quad (2)$$

where $\delta(\mathbf{x})$ denotes the three-dimensional Dirac distribution. We assume that the points \mathbf{y}_j are contained in a finite computational domain $B \equiv [-1, 1]^3$ and that the solution is sought within B as well. In particular, we focus on the efficient evaluation of $u(\mathbf{x}, t)$ at a large number of spatial targets $\mathbf{x} \in B$, for a set of discrete time slices $t \in (0, T]$.

The problem (1) can be solved exactly using the free-space Green's function for the wave equation (the *wave kernel*) [1], given by

$$G(\mathbf{x}, t) = \frac{\delta(t - |\mathbf{x}|)}{4\pi |\mathbf{x}|}, \quad (3)$$

where $\delta(t)$ denotes the one-dimensional Dirac distribution. The exact solution to (1) is the space-time convolution

$$u(\mathbf{x}, t) = \int_0^t \int_{\mathbb{R}^3} G(\mathbf{x} - \mathbf{y}, t - \tau) f(\mathbf{y}, \tau) d\mathbf{y} d\tau. \quad (4)$$

Given the fact that the forcing function takes the form (2), then using the δ -function form of the Green's function (a manifestation of the strong Huygens' principle), we may write

$$u(\mathbf{x}, t) = \sum_{j=1}^M \int_0^t G(\mathbf{x} - \mathbf{y}_j, t - \tau) \sigma_j(\tau) d\tau \quad (5)$$

$$= \sum_{j=1}^M \frac{\sigma_j(t - |\mathbf{x} - \mathbf{y}_j|)}{4\pi |\mathbf{x} - \mathbf{y}_j|}, \quad \mathbf{x} \neq \mathbf{y}_j, j = 1, \dots, M. \quad (6)$$

Direct evaluation of this retarded potential at M targets at a single time t clearly has cost $\mathcal{O}(M^2)$. (In an integral equation setting, such an evaluation would be needed at each time step.)

Rather than making direct use of the free-space Green's function, as above, it is tempting to solve (1) using Fourier analysis. For this, we define the spatial Fourier transform pair by

$$\hat{u}(\mathbf{k}, t) = \int_{\mathbb{R}^3} u(\mathbf{x}, t) e^{i\mathbf{k} \cdot \mathbf{x}} d\mathbf{x}, \quad \text{and} \quad u(\mathbf{x}, t) = \frac{1}{(2\pi)^3} \int_{\mathbb{R}^3} \hat{u}(\mathbf{k}, t) e^{-i\mathbf{k} \cdot \mathbf{x}} d\mathbf{k}. \quad (7)$$

Fourier transformation of the scalar wave equation (1) itself results in the ordinary differential equation (ODE)

$$\partial_t^2 \hat{u}(\mathbf{k}, t) + \kappa^2 \hat{u}(\mathbf{k}, t) = S(\mathbf{k}, t), \quad (8)$$

where (here and throughout the paper) $\kappa := |\mathbf{k}|$ denotes the wavevector magnitude. The right-hand side driving $S(\mathbf{k}, t)$ is the spatial Fourier transform of the source f . In our spatially discretized setting with the latter given by (2), we have

$$S(\mathbf{k}, t) = \sum_{j=1}^M \sigma_j(t) e^{i\mathbf{k} \cdot \mathbf{y}_j}. \quad (9)$$

Solution of the ODE at each \mathbf{k} by Duhamel's principle leads to the spectral representation

$$u(\mathbf{x}, t) = \frac{1}{(2\pi)^3} \int_{\mathbb{R}^3} \int_0^t e^{-i\mathbf{k} \cdot \mathbf{x}} \frac{\sin \kappa(t - \tau)}{\kappa} S(\mathbf{k}, \tau) d\tau d\mathbf{k}. \quad (10)$$

By comparing (10) and (4), or by direct computation of $\hat{G}(\mathbf{k}, t)$, one finds that the spectral representation of the wave kernel is

$$G(\mathbf{x}, t) = \frac{1}{(2\pi)^3} \int_{\mathbb{R}^3} \frac{\sin \kappa t}{\kappa} e^{-i\mathbf{k} \cdot \mathbf{x}} d\mathbf{k}, \quad t > 0. \quad (11)$$

At first glance, the Fourier-based solution (10) is of little numerical interest for three simple reasons. First, the wavevector integrand is slowly decaying (note that the wave kernel decays like $1/\kappa$ while S

does not decay at all);¹ this is associated with the non-smooth “switch on” of the response at $\tau = t$. Second, this integrand becomes more and more oscillatory as time advances, so that a finer and finer volumetric discretization of \mathbf{k} is needed as $t \rightarrow \infty$. Third, the representation is still dependent on the entire space-time history of f . It turns out, however, that all three of these obstacles can be overcome, leading to our fast algorithm.

The first concern is addressed by the windowed Fourier projection (WFP) method, introduced by the authors in [15], which ensures that the integrand in (10) is rapidly decaying with respect to \mathbf{k} , so long as one limits the Fourier representation to the “history part” of the solution. More precisely, in the WFP approach, we split the solution (5) into a non-smooth local part, u_l , plus a smooth history part, u_h , using a temporal blending function, ϕ :

$$u_l(\mathbf{x}, t) = \int_{t-\delta}^t \sum_{j=1}^M G(\mathbf{x} - \mathbf{y}_j, t - \tau) \sigma_j(\tau) [1 - \phi(t - \tau)] d\tau, \quad (12a)$$

$$u_h(\mathbf{x}, t) = \int_0^t \sum_{j=1}^M G(\mathbf{x} - \mathbf{y}_j, t - \tau) \sigma_j(\tau) \phi(t - \tau) d\tau, \quad (12b)$$

with $u = u_l + u_h$. The function ϕ , defined in the next section, is (numerically) smooth, with $\phi(t) = 0$ for $t \leq 0$, and $\phi(t) = 1$ for $t \geq \delta$. Its parameter $\delta > 0$ is chosen to be of order the shortest timescale present in the signatures σ_j . This split is illustrated in Fig. 1 (specifically the upper region with $\tau \in [t - \delta, t]$). The shape of ϕ depends on precision parameter $\epsilon > 0$, and is designed so that its ϵ -bandlimit² is as small as possible; this will scale as $\mathcal{O}(|\log \epsilon|/\delta)$. The local part u_l involves interactions only up to distance δ , so that (12a) can be computed directly—typically in linear time—using suitable quadrature rules. The history part u_h is evaluated as a spectral representation ((10) modified by a factor $\phi(t - \tau)$ in the integrand) that, due to the blending, may be truncated with error $\mathcal{O}(\epsilon)$ to $|\mathbf{k}| \leq K$ where K is similar to the signal ϵ -bandlimit. The fast evaluation of u_h relies on the non-uniform fast Fourier transform (NUFFT) and overcomes the history-dependence by exploiting the semigroup property of the governing wave equation. Specifically, a discretized set of Fourier coefficients of u_h will be updated by time-marching to arbitrarily high order accuracy, with a uniform time-step Δt that need only be slightly smaller than the time-step needed to resolve the signatures σ_j themselves.

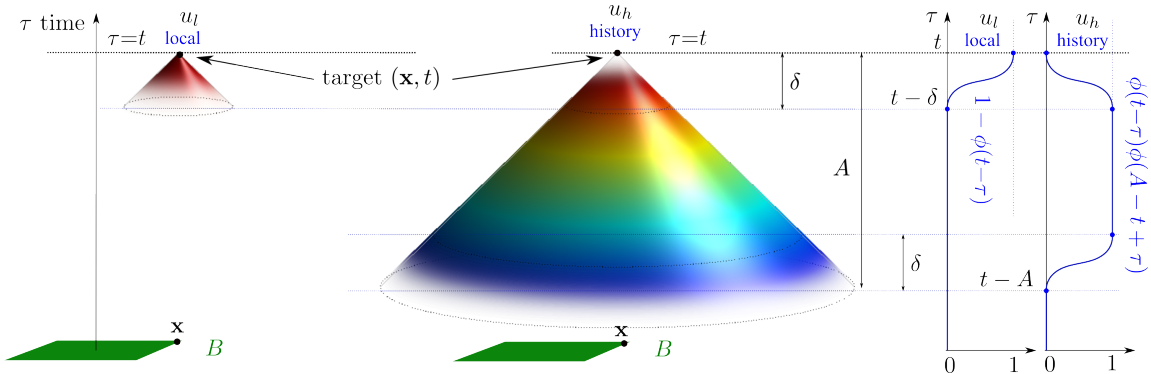


Figure 1: Local and truncated history contributions to the solution $u(\mathbf{x}, t)$ at a target location $\mathbf{x} \in B = [-1, 1]^3$ at the current time t . The left side depicts the space-time diagram (light cone) for the local u_l part, while the central image is the same for the history u_h part. The vertical axis shows the source time τ spanning 0 to the current slice t , and is common to all parts of the figure. (Only two of the three dimensions of space are shown; each temporal slice of the light “cone” is a sphere rather than a circle.) The color on the cones $|\mathbf{x} - \mathbf{y}| = t - \tau$ indicates the delay $t - \tau$. The right side graphs their respective temporal windowing functions; see (12a) for the local part, and (17) for the history part where the kernel \mathcal{G}_A is smoothly truncated to the finite time horizon $t - \tau < A$. Note that $A - \delta \geq \text{diam } B$, so that this truncation has no effect in B .

In its original form, the WFP method was derived for a periodic box, avoiding the need to consider the oscillatory nature of the integrand in the Fourier integral (the second concern above). Motivated

¹A more detailed analysis shows that, for σ_j smooth, after performing the time integral, the wavevector integrand decays as $1/\kappa^2$. Truncation of this integral would thus still result in slow convergence.

²The ϵ -bandlimit of a function f is defined as the smallest frequency ω such that $\|\hat{f}\|_{L^2(\mathbb{R} \setminus [-\omega, \omega])} \leq \epsilon$.

by the truncated kernel method of [16] for elliptic PDEs, we extend the WFP method here by using a *spatially truncated* version of the wave kernel, which we will denote by \mathcal{G}_A . The essential requirement is that $\mathcal{G}_A(\mathbf{x} - \mathbf{y}, t)$ coincide with $G(\mathbf{x} - \mathbf{y}, t)$ for all $\mathbf{x}, \mathbf{y} \in B$, $t \in \mathbb{R}$. Equivalently, the Green's functions must coincide in a double-sized cubical domain:

$$\mathcal{G}_A(\mathbf{x}, t) = G(\mathbf{x}, t) \quad \text{for all } \mathbf{x} \in [-2, 2]^3, t \in \mathbb{R}. \quad (13)$$

Radial truncation is extremely convenient since it allows the passage from spatial to temporal truncation, due to strong Huygens, as follows. We define

$$\mathcal{G}_A(\mathbf{x}, t) := \phi(A - |\mathbf{x}|)G(\mathbf{x}, t) = \phi(A - t)G(\mathbf{x}, t), \quad (14)$$

where we choose the same blending function ϕ and same parameter δ as for the WFP splitting, in order allow the same Fourier truncation $|\mathbf{k}| \leq K$, and set the history support parameter

$$A = 2\sqrt{3} + \delta. \quad (15)$$

One may check (using the fact that $\phi(t) = 1$ for $t \geq \delta$) that this value is the smallest choice of A for which (13) holds. From the last expression in (14) we immediately see that the (spatial) Fourier transform of $\mathcal{G}_A(\mathbf{x}, t)$ is

$$\hat{\mathcal{G}}_A(\mathbf{k}, t) = \phi(A - t) \frac{\sin \kappa t}{\kappa}, \quad t > 0. \quad (16)$$

Substituting the truncated kernel for the free-space Green's function $G(\mathbf{x}, t)$ in the Fourier transform domain, using (16), gives

$$u_h(\mathbf{x}, t) = \frac{1}{(2\pi)^3} \int_{\mathbb{R}^3} \int_{t-A}^t e^{-i\mathbf{k} \cdot \mathbf{x}} \frac{\sin \kappa(t - \tau)}{\kappa} S(\mathbf{k}, \tau) \phi(t - \tau) \phi(A - t + \tau) d\tau d\mathbf{k}, \quad (17)$$

which combines the blended ‘‘switch on’’ of WFP with the blended ‘‘switch off’’ of kernel truncation, as sketched in the right-most graph in Fig. 1. Note the change in lower time limit, since $\phi(A - t + \tau) = 0$ for $\tau < t - A$: the time horizon is now finite. The finite spatial extent of the truncated kernel now controls the integrand's oscillation rate with respect to \mathbf{k} , so that using a Nyquist-spaced trapezoid quadrature needs a wavenumber grid spacing of only $\mathcal{O}(1)$, no matter how large t is.

In short, the truncated-kernel WFP (TK-WFP) method approximates the solution (4) to spectral accuracy by a splitting into a history and local part, with the history part computed in the Fourier transform domain using $N = \mathcal{O}(1/\Delta t)$ quadrature nodes per dimension, and the local part computed directly. The amount of work required is $\mathcal{O}(M + N^3 \log N)$ per time-step, dominated by the NUFFT. $N_t = T/\Delta t$ such steps are needed to reach the final simulation time T . The storage requirements for the scheme as we present it are greater than for the original WFP method, since we will need to keep track of the time history for each source over the horizon $[t - A, t]$ (see Remark 4.2). The splitting is discussed in detail in section 2, the history part in sections 3 and 4, and the local part in section 5. Section 6 illustrates the performance of the scheme with several numerical examples. We conclude with a brief discussion in Section 7. Two appendices contain the proof of the main theoretical result (Theorem 1) on spectral decay of Fourier coefficients.

1.1. Prior work

While we do not seek to present a thorough review of the literature, it should be noted that a variety of algorithms have been developed to rapidly evaluate sums of the form (4) at N_t time steps in $\mathcal{O}(N_t M \log^2 M)$ operations. Of particular relevance is the plane-wave time domain method (PWTD) of Ergin, Shanker, Michielssen and collaborators [9, 13, 17], a time-domain version of the fast multipole method. It achieves more or less optimal asymptotic performance, independent of whether the sources lie on a surface or are more uniformly distributed in the computational domain. In [18], Meng et al. present an alternative that is easier to implement, relying on an adaptive Cartesian grid and sparse interpolation methods to compute far-field interactions rather than relying on spherical harmonic expansions. A related acceleration technique is the fast convolution quadrature algorithm of [6], which combines the Laplace transform with \mathcal{H} -matrices and the high-frequency fast-multipole method to achieve the same complexity.

Because the associated constants are rather large, however, the design of such fast algorithms remains an active area of research. One such scheme is the time-domain adaptive integral method [5] which, like ours, is an FFT-based scheme, but does not evolve the Fourier transform of the solution. Instead relying on the fact that the wave kernel is convolutional in space and time, it uses multilevel, blocked space-time FFTs. For layer potentials on surfaces, the cost is of the order $\mathcal{O}(N_t M^{3/2} \log M)$ operations. It is simpler to implement than the PWTD algorithm, with smaller associated constants but suboptimal asymptotic scaling. The same is true for the method presented here.

Recently, hybrid time-frequency approaches have been proposed that can achieve excellent performance under suitable conditions on the data. These include [19, 20] and the recent work of Wilber et al. [21]. The latter combines contour deformation and the fast sinc transform to overcome the oscillatory nature of the wave kernel in the Fourier transform domain. Like the scheme of [6] mentioned above, it makes use of fast solvers for a sequence of Helmholtz equations, rather than a marching scheme in the time domain.

There is also, of course, a vast literature on solving the wave equation by direct discretization of the governing equation using finite difference or finite element methods (e.g., [10, 14, 22]), combined with “non-reflecting” or “absorbing” boundary conditions on a finite computational domain. Such boundary conditions are generally designed as local approximations of the exact non-local exact radiation condition. Examples of such conditions include those by Engquist and Majda [23], Bayliss and Turkel in [24], and Higdon [25]. These methods are generally low order accurate and tend to lose precision for waves that are not normally incident to the artificial boundary. For greater precision, absorbing region methods have been developed that minimize numerical reflection by modifying the governing PDE itself by adding a damping term [26], or by a coordinate transformation, such as the Perfectly Matched Layer (PML) method [27]. We refer the reader to the review articles [28–30] for further details. Ongoing work in that direction includes ideas from numerical relativity [31] and geophysics [32]. More recently, the double absorbing boundary (DAB) method and complete radiation boundary conditions (CRBC) were introduced by Hagstrom, Warburton and Givoli [33–36], which are able to accurately approximate the exact radiation condition to a specified error tolerance. They are especially convenient for coupling to finite difference methods because they can be applied on rectangular boxes of arbitrary aspect ratio. Exact outgoing conditions have also been developed for spherical boundaries [37, 38].

Finally, we should note the methods of Global Discrete Artificial Boundary Conditions [39] and Time-Dependent Phase Space Filters [40–42]. The former relies on the strong Huygens’ principle and requires the solution of an auxiliary problem on a larger domain. The latter detects microlocally outgoing components of the solution and deletes them from the representation using the Fourier transform at periodic intervals in time. Both can be carried out with high precision.

Note that our proposal’s cost per timestep of $\mathcal{O}(N^3 \log N)$, N being the highest frequency, is, up to the log factor, the same order as that of a finite difference or element discretization with a fixed number of grid-points per wavelength. The latter is well known to suffer from dispersion errors unless the order is very high [14, 43] [22, §4.6]. A major advantage of our method is that it achieves global spectral accuracy, without dispersion error, through the use of the discretized Fourier transform.

2. Windowed Fourier projection and the decomposition of hyperbolic potentials

The windowed Fourier projection method (WFP) [15] is based on a numerically smooth partition of unity using a blending function $\phi(t)$, with $\phi(t) = 0$ for $t \leq 0$ and $\phi(t) = 1$ for $t \geq \delta$, with the small parameter $\delta > 0$ chosen of order the time-step. Its precise value will be adjusted to balance the local and history computational effort.

2.1. The blending function

As in [15], we exploit the Kaiser–Bessel “bump” function $I_0(b\sqrt{1-t^2})$, $t \in [-1, 1]$, where I_0 is the zeroth-order modified Bessel function, while $b = \ln(1/\epsilon)$ is a shape parameter. This bump function has many applications in signal and image processing. Its peak width scales as $b^{-1/2}$ while its peak value scales as e^b . This is shifted and scaled to a unit-integral bump on the domain $[0, \delta]$, and its antiderivative is taken:

$$\phi(t) := \int_0^t \phi'(\tau) d\tau, \quad \text{where} \quad \phi'(t) := \begin{cases} \frac{b}{\delta \sinh b} I_0\left(b\sqrt{1-(2t/\delta-1)^2}\right), & 0 \leq t \leq \delta, \\ 0, & t < 0 \text{ or } t > \delta. \end{cases} \quad (18)$$

This satisfies the following properties.

1. The function ϕ transitions smoothly from 0 to 1 in $[0, \delta]$. It is formally non-smooth on \mathbb{R} , there being an $\mathcal{O}(e^{-b})$ jump in ϕ' at $t = 0$ and $t = \delta$. Thus the choice $b = \ln(1/\epsilon)$, for $\epsilon \ll 1$, ensures that ϕ is *numerically* smooth up to tolerance ϵ .
2. The Fourier transform of ϕ' is available analytically:

$$\hat{\phi}'(\omega) := \int_{\mathbb{R}} \phi'(t) e^{i\omega t} dt = \frac{b e^{-i\delta\omega/2}}{\sinh b} \operatorname{sinc} \sqrt{\left(\frac{\delta\omega}{2}\right)^2 - b^2}, \quad \omega \in \mathbb{R}, \quad (19)$$

where $\operatorname{sinc}(z) := \sin(z)/z$ for $z \neq 0$ and 1 otherwise. The $\mathcal{O}(\epsilon)$ -support of $\hat{\phi}'$ is $[-2b/\delta, 2b/\delta]$, as one may see by noting that the argument of the sinc is real outside of this domain (the sinc is exponentially large in the domain). In other words, the ϵ -bandlimit of ϕ' is $2b/\delta$.

Elaborating on the second property, we will need the following decay bound beyond the bandlimit, which is proved in [Appendix A](#).

Lemma 2.1. *Let $\delta > 0$ and $0 < \epsilon < 1$. Then (19) with $b = \ln(1/\epsilon)$ obeys, for any $\theta > 1$, the bound*

$$|\hat{\phi}'(\omega)| < \frac{4b\theta}{\delta} \cdot \frac{\epsilon}{|\omega|}, \quad \text{for all } |\omega| \geq \frac{2b}{\delta\sqrt{1-1/\theta^2}}. \quad (20)$$

2.2. The local and history part

Recall that the solution is represented as $u(\mathbf{x}, t) = u_l(\mathbf{x}, t) + u_h(\mathbf{x}, t)$, with the local part defined by (12a) and the history part

$$u_h(\mathbf{x}, t) = \sum_{j=1}^M \int_0^t \mathcal{G}_A(\mathbf{x} - \mathbf{y}_j, t - \tau) \sigma_j(\tau) \phi(t - \tau) d\tau, \quad (21)$$

where \mathcal{G}_A is the truncated kernel (14).

The local part (12a) involves an integral over the most recent times, and can be treated directly as in (6) but for a spatially restricted region around each target:

$$u_l(\mathbf{x}, t) = \sum_{j \in \mathcal{N}_\delta(\mathbf{x})} \frac{\sigma_j(t - r_j) [1 - \phi(r_j)]}{4\pi r_j}, \quad (22)$$

with the abbreviation $r_j := |\mathbf{x} - \mathbf{y}_j|$, and the neighbor index set definition $\mathcal{N}_\delta(\mathbf{x}) := \{j \mid 0 < r_j < \delta, j = 1, 2, \dots, M\}$. Note that we use $G(\mathbf{x}, t)$ in (12a) since for short times it is equal to $\mathcal{G}_A(\mathbf{x}, t)$, for all $\mathbf{x} \in B$, because $\delta < A - \delta$. The high-order quadrature approximation of u_l is then routine, and we postpone it to Section 5.

The history part of the solution, u_h , on the other hand, will be expressed as the Fourier integral

$$u_h(\mathbf{x}, t) = \frac{1}{(2\pi)^3} \int_{\mathbb{R}^3} \alpha(\mathbf{k}, t) e^{-i\mathbf{k} \cdot \mathbf{x}} d\mathbf{k}, \quad (23)$$

with coefficients from (17) given by

$$\alpha(\mathbf{k}, t) = \int_{t-A}^t \frac{\sin \kappa(t - \tau)}{\kappa} S(\mathbf{k}, \tau) \phi(t - \tau) \phi(A - t + \tau) d\tau, \quad (24)$$

recalling the Fourier source function $S(\mathbf{k}, \tau)$ defined in (9). Its numerical approximation and fast computation occupies the next two sections.

3. Approximation of the history part and choice of δ

3.1. Discretization of the Fourier integral

The Fourier integral (23) for u_h may be discretized using the 3D infinite trapezoidal rule with equal step size Δk :

$$u_h(\mathbf{x}, t) = \frac{1}{(2\pi)^3} \int_{\mathbb{R}^3} \alpha(\mathbf{k}, t) e^{-i\mathbf{k}\cdot\mathbf{x}} d\mathbf{k} \approx \left(\frac{\Delta k}{2\pi}\right)^3 \sum_{\mathbf{n} \in \mathbb{Z}^3} \alpha(\mathbf{n}\Delta k, t) e^{-i\mathbf{n}\Delta k \cdot \mathbf{x}}, \quad \mathbf{x} \in B. \quad (25)$$

Deferring the issue of truncation of this infinite sum to the next subsection, we first discuss the discretization error. Remarkably, once Δk is below an explicit $\mathcal{O}(1)$ constant, there is no such error.

Proposition 3.1. *Let $\Delta k \leq 2\pi/(A+2)$, recalling (15), and let the coefficients $\alpha(\mathbf{k}, t)$ be given by (24) with $S(\mathbf{k}, \tau)$ given by (9). Then the discretization error is zero, that is, (25) is an equality.*

The proof relies on the finite spatial support of \mathcal{G}_A , as follows. Shifting and scaling the 3D version of the Poisson summation formula (e.g., [44, Ch. VII, Cor. 2.6]) gives

$$\left(\frac{\Delta k}{2\pi}\right)^3 \sum_{\mathbf{n} \in \mathbb{Z}^3} \alpha(\mathbf{n}\Delta k, t) e^{-i\mathbf{n}\Delta k \cdot \mathbf{x}} = u_h(\mathbf{x}, t) + \sum_{\mathbf{m} \in \mathbb{Z}^3 \setminus \{\mathbf{0}\}} u_h\left(\mathbf{x} + \frac{2\pi}{\Delta k} \mathbf{m}, t\right).$$

The error is the 2nd term on the right-hand side. Since $\mathbf{y}_j \in B$ for all j , while the spatial support of \mathcal{G}_A (recalling (14)) lies within the ball of radius A , the spatial support of $u_h(\cdot, t)$ lives within the cube $[-A-1, A+1]^3$. Yet for $\mathbf{x} \in B$, each spatial argument $\mathbf{x} + (2\pi/\Delta k)\mathbf{m}$ lies outside of this cube, since $2\pi/\Delta k \geq A+2$. Thus each term on the right-hand side sum is zero, and so is the error.

This result may also be interpreted as the exactness of the periodic trapezoid quadrature when applied to an integrand that has bandlimit (with respect to each component of \mathbf{k}) no more than $2\pi/\Delta k$. (For the periodic case see, for example, [45, Cor. 3.3].) Given the above, in practice we set

$$\Delta k \approx \frac{2\pi}{A+2}, \quad (26)$$

which is about 1.15 when $\delta \ll 1$.

3.2. Wavenumber truncation

Next we determine a cut-off wavenumber magnitude K such that truncation of the above sum to the ball $|\mathbf{k}| \leq K$ incurs error of only $\mathcal{O}(\epsilon)$, where ϵ is a user-chosen tolerance. This is supplied by the following.

Theorem 1. *Let $\sigma_j \in L_2(\mathbb{R}_+)$, with $\|\sigma_j\|_1 \leq P$, $j = 1, \dots, M$, be given source signature functions. Let the tolerance $0 < \epsilon < 1$ and numerical bandlimit K_0 be such that the Fourier transforms $\hat{\sigma}_j(\omega)$ decay as*

$$|\hat{\sigma}_j(\omega)| \leq \frac{\epsilon}{\omega^2}, \quad \text{for all } |\omega| > K_0. \quad (27)$$

Let the blending timescale be $\delta > 0$, then let ϕ be defined as in (18) with $b = \ln(1/\epsilon)$. Then, for each $\theta > 1$, the Fourier coefficients defined by (24) obey the decay condition

$$|\alpha(\mathbf{k}, t)| = \frac{CM\epsilon}{\kappa^3}, \quad \text{for all } \kappa > K := K_0 + \frac{2b}{\delta\sqrt{1-1/\theta^2}}, \quad t \in [0, T], \quad (28)$$

recalling the notation $\kappa := |\mathbf{k}|$. Here C is some constant independent of ϵ , that depends only weakly on K_0 , b , δ , θ , and P .

This implies that the coefficients $\alpha(\mathbf{k}, t)$ are of size $\mathcal{O}(\epsilon)$, with rapid algebraic decay, beyond a numerical wavenumber cut-off K . This cut-off need only be slightly larger than the ϵ -bandlimit K_0 of the given signals plus the ϵ -bandlimit $2b/\delta$ of the blending function. (By choosing θ sufficiently large, K may be pushed arbitrarily close to this sum at the cost of only mild growth in the error prefactor.)

The proof of the above theorem is given in Appendix B, which also states the explicit formula for C in (28). The proof combines the decay of the signals outside their ϵ -bandwidth K_0 , the decay of

$\hat{\phi}'$ outside its ϵ -bandwidth (Lemma 2.1), the convolution theorem, and the fact that the wave kernel $\sin[\kappa(t - \tau)]/\kappa$ converts temporal to spatial bandlimitness. The technical condition (27) is merely a convenient expression of the signal being ϵ -bandlimited; Gaussians and other common smooth signals will have tails that decay faster than quadratically in ω . Note that, although one could prove a much simpler theorem by assuming that σ_j is *strictly* bandlimited (hence analytic on \mathbb{R}), this assumption would only admit trivial data $\sigma_j \equiv 0$ via the need for $\sigma_j(t) = 0$ for all $t < 0$; such a theorem would not be interesting!

Remark 3.1 (Bound on the truncation error). *Although Theorem 1 shows that the coefficients $\alpha(\mathbf{k}, t)$ are uniformly $\mathcal{O}(\epsilon)$ in $|\mathbf{k}| \geq K$, unfortunately their $1/\kappa^3$ wavenumber decay rate is not quite fast enough to prove summability of the error $\sum_{\mathbf{n} \in \mathbb{Z}^3: |\mathbf{n}\Delta k| > K} \alpha(\mathbf{n}\Delta k, t) e^{-i\mathbf{n}\Delta k \cdot \mathbf{x}}$ induced by truncation in $d = 3$ dimensions, at least not via a bound on $|\alpha|$. This limitation is due to the $\epsilon/|\omega|$ tail bound for $\hat{\phi}'$, in turn tied to the $\mathcal{O}(\epsilon)$ discontinuities in ϕ' at 0 and δ . One may be able to fix this theoretical deficit by switching to the “deplinthed” (continuous) Kaiser–Bessel window as in [46]. However, the numerical performance is expected to be almost identical.*

Motivated by the above theorem, we thus truncate the infinite sum (25) to the finite ball $|\mathbf{k}| \leq K$, whose radius in practice we set as

$$K = K_0 + \frac{2b}{\delta}, \quad (29)$$

the large- θ limit of (28). Thus, combining the results of this section so far, with the above choices of Δk , b , and K , we expect that u_h is approximated to error $\mathcal{O}(\epsilon)$ by the discrete sum

$$u_h(\mathbf{x}, t) \approx \left(\frac{\Delta k}{2\pi}\right)^3 \sum_{\mathbf{n} \in \mathbb{Z}^3: |\mathbf{n}\Delta k| \leq K} \alpha(\mathbf{n}\Delta k, t) e^{-i\mathbf{n}\Delta k \cdot \mathbf{x}}, \quad \mathbf{x} \in B. \quad (30)$$

3.3. Choice of blending timescale

Given the tolerance ϵ and the signal ϵ -bandwidth K_0 , it remains to set the blending parameter δ . As in [15], we set $\delta = W\Delta t$, where Δt the time-step with which the history coefficients are evolved, and W is a small integer. We choose

$$W := \left\lceil \frac{2b}{\pi\gamma} \right\rceil, \quad (31)$$

where $\gamma \in (0, 1)$ is a dimensionless parameter, and note that W grows as $\log(1/\epsilon)$ as more precision is demanded. We then have $2b/\delta \approx \pi\gamma/\Delta t$. Thus (29) becomes $K \approx K_0 + \frac{\pi\gamma}{\Delta t}$. This indicates that γ is the fraction of the time-step Nyquist bandlimit $\pi/\Delta t$ sacrificed to the blending function, the remaining fraction being accounted for by the signal bandlimit K_0 . Note that reducing γ decreases K and, therefore, the cost associated with the history part, but increases W and δ and, therefore, the amount of work required in the local part. Thus, γ can be used to adjust the history/local workload balance. We typically choose $\gamma \approx 0.5$.

Note also that if Δt were set much smaller than the Nyquist value for the signal, π/K_0 , the bandlimit (hence cost) of the history part would be excessively large. Fortunately, with a high order method, the solution converges rapidly once $\Delta t < \pi/K_0$. Setting $\Delta t = \pi/(2K_0)$, for example, with $\gamma = 0.5$, results in $K = 2K_0$, an acceptable increase in the bandlimit.

4. Computation of the history part

The reason that the history part can be evaluated efficiently is that the Fourier coefficients $\alpha(\mathbf{k}, t)$ satisfy evolution formulae and can be computed recursively at each time step. In particular, it is easy to check that, independently at each wavenumber \mathbf{k} , they satisfy the ODE initial value problem

$$\begin{cases} \ddot{\alpha}(\mathbf{k}, t) + \kappa^2 \alpha(\mathbf{k}, t) = F(\mathbf{k}, t), & t > 0, \\ \alpha(\mathbf{k}, 0) = \dot{\alpha}(\mathbf{k}, 0) = 0, \end{cases} \quad (32)$$

using the notation $\dot{\alpha} := \partial_t \alpha$, with forcing

$$F(\mathbf{k}, t) = \int_{t-\delta}^t [\Psi(\mathbf{k}, t-\tau)S(\mathbf{k}, \tau) - \Psi_A(\mathbf{k}, t-\tau)S(\mathbf{k}, \tau - A + \delta)] d\tau, \quad (33)$$

where

$$\begin{aligned}\Psi(\mathbf{k}, \tau) &:= 2 \cos \kappa \tau \phi'(\tau) + \frac{\sin \kappa \tau}{\kappa} \phi''(\tau), \\ \Psi_A(\mathbf{k}, \tau) &:= 2 \cos \kappa(\tau + A - \delta) \phi'(\tau) + \frac{\sin \kappa(\tau + A - \delta)}{\kappa} \phi''(\tau).\end{aligned}\tag{34}$$

This is done for each discrete $\mathbf{k} = \mathbf{n}\Delta k$ with $|\mathbf{k}| \leq K$, as in the previous section. In these and the below expressions, the case $\mathbf{k} = \mathbf{0}$ is taken as the limit $\kappa \rightarrow 0$, so that $(\sin \kappa \tau)/\kappa$ becomes τ , etc.

Remark 4.1. We refer to Ψ as the *creation kernel*, since it is responsible for injecting contributions to $\alpha(\mathbf{k}, t)$ near the current time t to balance the disappearing local part; this is as in [15]. We refer to the new term Ψ_A as the *annihilation kernel* since it is responsible for removing the historical contributions to $\alpha(\mathbf{k}, t)$ from times earlier than $t - A$.

The solution to (32) at each \mathbf{k} is

$$\alpha(\mathbf{k}, t) = \int_0^t \frac{\sin \kappa(t - \tau)}{\kappa} F(\mathbf{k}, \tau) d\tau.\tag{35}$$

One may thus interpret (33) as the driving such that the coefficients α obey the simple 2nd-order ODE (32), enabling the standard Duhamel-type solution (35) in contrast to the windowed evaluation formula (24).

The following can be easily derived from (35), or from the Duhamel principle applied to the ODE (32).

Lemma 4.1. Let $\Delta t > 0$ denote a time step. The Fourier coefficients $\alpha(\mathbf{k}, t)$ satisfy the evolution formulae

$$\begin{aligned}\alpha(\mathbf{k}, t + \Delta t) &= \alpha(\mathbf{k}, t) \cos(\kappa \Delta t) + \dot{\alpha}(\mathbf{k}, t) \frac{\sin \kappa \Delta t}{\kappa} + h(\mathbf{k}, t), \\ \dot{\alpha}(\mathbf{k}, t + \Delta t) &= -\kappa \alpha(\mathbf{k}, t) \sin(\kappa \Delta t) + \dot{\alpha}(\mathbf{k}, t) \cos \kappa \Delta t + g(\mathbf{k}, t),\end{aligned}\tag{36}$$

where

$$h(\mathbf{k}, t) := \int_t^{t+\Delta t} \frac{\sin \kappa(t + \Delta t - \tau)}{\kappa} F(\mathbf{k}, \tau) d\tau, \quad g(\mathbf{k}, t) := \int_t^{t+\Delta t} \cos \kappa(t + \Delta t - \tau) F(\mathbf{k}, \tau) d\tau.\tag{37}$$

Thus by storing the pair α and $\dot{\alpha}$ at each \mathbf{k} , their exact update over one time step takes the form of a 2×2 matrix-vector multiply plus a known vector.

Gauss–Legendre quadrature over the interval $[t, t + \Delta t]$ can be used to approximate h and g in (37) to high order accuracy. In turn the integral over $[t - \delta, t]$ needed for F in (33) may be approximated using the trapezoid rule on the time-stepping grid itself. By exchanging the order of these integrals, one may precompute weights $p_m(\mathbf{k})$ and $q_m(\mathbf{k})$ such that for a current time t on the time grid,

$$\begin{aligned}h(\mathbf{k}, t) &\approx \Delta t \sum_{m=0}^{W-1} p_m(\mathbf{k}) S(\mathbf{k}, t - m\Delta t) - p_m^{(A)}(\mathbf{k}) S(\mathbf{k}, t - A + \delta - m\Delta t), \\ g(\mathbf{k}, t) &\approx \Delta t \sum_{m=0}^{W-1} q_m(\mathbf{k}) S(\mathbf{k}, t - m\Delta t) - q_m^{(A)}(\mathbf{k}) S(\mathbf{k}, t - A + \delta - m\Delta t),\end{aligned}\tag{38}$$

holds to high order accuracy. See [15, §3] for the formulae for p and q ; the formulae for $p^{(A)}$ and $q^{(A)}$ are analogous. Values of S for $t < 0$ are assumed to be zero.

4.1. Computation and storage costs

At each time step, $S(\mathbf{k}, t)$ must be computed from (9), for all wavevectors on the grid $\mathbf{k} = \mathbf{n}\Delta k$, $\mathbf{n} \in \mathbb{Z}^3$, with $|\mathbf{k}| \leq K$. This is approximated to relative tolerance ϵ by a single application of a NUFFT (Non-Uniform fast Fourier transform) of type 2 [47, 48], outputting the cube of N^3 coefficients where $N := \lceil \frac{2K}{\Delta k} \rceil$ is the maximum number of wavevector quadrature points per dimension. The values with wavevectors in this cube but outside the ball $|\mathbf{k}| = K$ are then set to zero. This NUFFT requires

$\mathcal{O}(\log^3(1/\epsilon)M + N^3 \log N)$ work. The subsequent calculation of $h(\mathbf{k}, t)$ and $g(\mathbf{k}, t)$ at each time step using (38) takes a linear combination of $S(\mathbf{k}, \tau)$ for τ ranging over the most recent W time-steps and the W time steps preceding $t - A$.

The Fourier coefficients $\alpha(\mathbf{k}, t)$ are then updated via (36). Finally, the evaluation of u_h via (30) at N_x target points $\{\mathbf{x}_i\}_{i=1}^{N_x}$ takes the form of a type 1 NUFFT, which can be performed at a cost $\mathcal{O}(\log^3(1/\epsilon)N_x + N^3 \log N)$ at each time step. Again, here the $\alpha(\mathbf{k}, t)$ values for $|\mathbf{k}| > K$ are padded to zero, since this NUFFT acts on a N^3 cubical input coefficient array.

Remark 4.2 (History storage costs). *Since the annihilation kernel is applied to historical data up to time A in the past, we need to store either $S(\mathbf{k}, \tau)$ for all time steps in the interval $[t - A, t]$, or the source signals $\sigma_j(\tau)$, from which $S(\mathbf{k}, \tau)$ can be reconstructed by a NUFFT on the fly. Data from time steps before time $t - A$ can be safely deleted. We note that regrouping via a partition of unity in time (as in, e.g., [39]) could much reduce this storage, at the cost of a slight increase in A .*

5. Computation of the local part

In this section we discuss the numerical computation of the local part of the solution, u_l , in (22):

$$u_l(\mathbf{x}_i, t) = \sum_{j \in \mathcal{N}_\delta(\mathbf{x}_i)} \frac{\sigma_j(t - r_{ij})[1 - \phi(r_{ij})]}{4\pi r_{ij}}, \quad (39)$$

for target points \mathbf{x}_i , $i = 1, \dots, N_x$, and source points \mathbf{y}_j , $j = 1, \dots, M$. Recall that $r_{ij} = |\mathbf{x}_i - \mathbf{y}_j|$, and $\mathcal{N}_\delta(\mathbf{x}_i)$ denotes the set of source indices with distances in $(0, \delta)$ from \mathbf{x}_i ; this excludes any sources that coincide with the target. Note that if $\mathbf{x}_i = \mathbf{y}_j$ for some source j , the above expression results in a total potential $u = u_l + u_h$ in (6) which excludes the self-interaction. Assuming that the densities σ_j are available at all retarded time values, $(t - r_{ij})$, we seek to express u_l at each target point as a dot product of two vectors. For this, we precompute the set

$$Q_{ij} = \frac{1 - \phi(r_{ij})}{4\pi r_{ij}}, \quad i = 1, \dots, N_x, \quad j \in \mathcal{N}_\delta(\mathbf{x}_i). \quad (40)$$

Then, at each new time t , these are used to weight the signal samples:

$$u_l(\mathbf{x}_i, t) = \sum_{j \in \mathcal{N}_\delta(\mathbf{x}_i)} \sigma_j(t - r_{ij})Q_{ij}, \quad i = 1, \dots, N_x. \quad (41)$$

The cost of computing u_l at N_x targets and M sources scales linearly with the typical number of sources within a δ -neighborhood of each target; the latter we denote by M_{typ} . The local cost for evaluation at a single time t is thus $\mathcal{O}(N_x M_{\text{typ}})$ flops. For a quasi-uniform volumetric distribution of sources and targets, $M_{\text{typ}} \approx 4\pi\delta^3 M / (3V_B)$, recalling the volume of the sphere of radius δ , and using $V_B = 8$, the volume of the computational domain B . For a quasi-uniform distribution on a surface, M_{typ} instead scales as $\delta^2 M$ for target points on the surface (relevant for the time-domain integral equation setting), while for distant off-surface evaluation one may have $M_{\text{typ}} = 0$.

Remark 5.1. *To find sources within $\mathcal{N}_\delta(\mathbf{x}_i)$ of a given target \mathbf{x}_i in a fast manner, one may sort source and target points into cubic boxes of side-length δ and search neighboring boxes only. For example, to evaluate u_l at a target point \mathbf{x}_i in box b_i , we find sources in $\mathcal{N}_\delta(\mathbf{x}_i)$ by searching the boxes that share a vertex, edge, or a face with b_i . This reduces the cost of the search for filling all elements of Q from $\mathcal{O}(N_x M)$ to $\mathcal{O}(\delta^3 N_x M)$.*

Remark 5.2. *For time-domain wave scattering schemes, σ_j may only be available on the uniform time grid. In this case, high-order interpolation from the uniform time grid is needed to approximate $\sigma_j(t - r_{ij})$, as in [15]. In the present paper, for simplicity, we assume that σ_j is a given function that may be rapidly evaluated at any argument.*

6. Numerical results

We present numerical examples to verify the high-order accuracy and computational performance of the TK-WFP algorithm. In Section 6.1, we demonstrate exponential convergence with respect to Δt ,

using a small number of source points. In Section 6.2, we investigate the algorithm’s performance in wave-scattering scenarios with many sources and targets covering a closed surface. Section 6.3 explores the accuracy and speed of the TK-WFP solution approach to a problem with a wide range of frequency settings and a large number of sources and targets.

In each of the numerical examples, we approximate the wave equation solution u to (1) using TK-WFP with a constant step size Δt . We denote the resulting approximate solution by \tilde{u} . We fix the error tolerance $\epsilon = 10^{-6}$. We measure the error at a given time t by evaluating the exact solution u directly using (6). We will report the maximum norm of the absolute, or relative error, defined respectively as

$$\mathcal{E}_{\Delta t} := \|\tilde{u} - u\|_{\infty}, \quad \tilde{\mathcal{E}}_{\Delta t} := \frac{\mathcal{E}_{\Delta t}}{\|u\|_{\infty}}, \quad (42)$$

for a particular Δt parameter. The norms are estimated as the maximum over a large number of target points \mathbf{x}_i at the final time $t = T$.

We clarify that evaluating the solution u at the last time slice $t = T$ requires computing the Fourier coefficients $\alpha(\mathbf{k}, n\Delta t)$, for each $|\mathbf{k}| \leq K$, on the regular grid $n = 0, 1, \dots, N_t$, recalling $N_t\Delta t = T$. We thus differentiate between *time steps* (of size Δt), with which these coefficients are evolved, and *time slices* t , where we choose to evaluate the full solution via $u = u_l + u_h$.

The TK-WFP and direct evaluations were implemented in MATLAB (version R2023b), with NUFFTs performed by calling the MATLAB interface to the C++ library FINUFFT (version 2.4.1). MATLAB sparse matrices were used to manipulate the set of entries Q_{ij} for the local part evaluation.

6.1. Convergence study

We begin with a simple example where we evaluate the solution representation u in (4) with a few point sources using the TK-WFP method, to test that the free-space radiative boundary conditions are correct. Let the source points \mathbf{y}_j be located at each of the eight corners $(\pm 1, \pm 1, \pm 1)$ of the cube B ; this excites the most severe grazing incident waves (these are known to be problematic when using approximate radiation boundary conditions). We choose identical time signatures

$$\sigma_j(t) = 0.5 [\operatorname{erf}(5(t - 1.5)) + 1] \sin(30\pi(t - 1.5)), \quad j = 1, 2, \dots, 8, \quad (43)$$

which take the form of a fixed high frequency at 30π modulated by a smooth “ramp up” erf blending function. At a tolerance $\epsilon = 10^{-6}$ the ϵ -bandlimit is $K_0 \approx 131$; this is 30π plus the ϵ -bandlimit of the erf. For the latter we use the estimate that the ϵ -bandlimit of $\operatorname{erf}(\mu t)$ is around $2\mu\sqrt{\log(1/\epsilon)}$, derived by the Fourier transform of its derivative (the Gaussian $e^{-(\mu t)^2}$, up to an $\mathcal{O}(1)$ prefactor). At the center signal frequency 30π , the size of the cube is 30 wavelengths on a side; at the bandlimit K_0 , this is 42 wavelengths. We fix the Nyquist fraction for the blending $\gamma = 0.5$. The width (31) of the blending region is then $W = 18$ time steps, recalling that $\delta = W\Delta t$.

Figure 2 (left) shows the computed solution \tilde{u} at a $100 \times 100 \times 100$ mesh of target points uniformly covering B , at a final time $T = 6$, and with time step $\Delta t = 0.0102$. Figure 2 (right) presents a 2D slice of that solution at $z = -0.01$. We observe clean outgoing waves at the boundary of B . The absolute error of this solution is $\mathcal{E}_{\Delta t} = 9.8 \times 10^{-7}$.

In Figure 3 we show, for the same example, convergence with respect to Δt of the absolute error. The error is estimated by evaluating $\tilde{u}(\mathbf{x}, t)$ over a $10 \times 10 \times 10$ uniform mesh of target points covering B , at $t = 6$. At each Δt , the maximum wavenumber is set as $K = \pi/\Delta t$, rather than fixing K using (29). The cut-off distance is $\delta = 0.1831$. The plot demonstrates spectral convergence of the TK-WFP method, down to saturation around the chosen 6-digit tolerance. The number of sources is too small to report meaningful CPU timings; for that we move to the following larger examples.

6.2. Sources and targets on a smooth surface

We demonstrate the computational performance of the TK-WFP algorithm compared to a naive direct evaluation in a setting where the source points are also the targets, and they lie on the boundary of a 3D surface. We encounter this evaluation task in time-domain integral-equation schemes for wave scattering problems from 3D obstacles.

We take $M = 102400$ source points with Gaussian pulse time signatures

$$\sigma_j(t) = 10 \exp[-\mu_j(t - t_{0,j})^2], \quad j = 1, \dots, M, \quad (44)$$

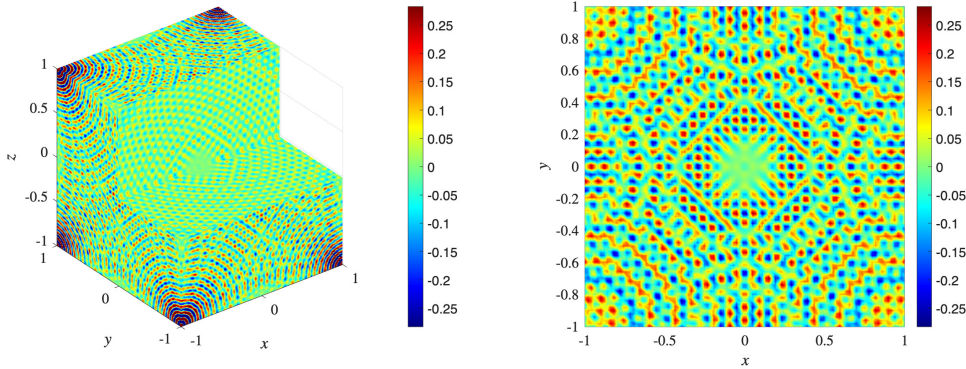


Figure 2: Computed solution due to eight sources as in Section 6.1, at time $t = 6$, using $\Delta t = 0.0102$. The same potential \bar{u} is shown as a cut-away of the volume (left), and on the plane $z = -0.01$ (right). At its center frequency (visible as the oscillations in the plot) the wave field has 30 wavelengths on each side of the cube B . The solution has 6 accurate digits.

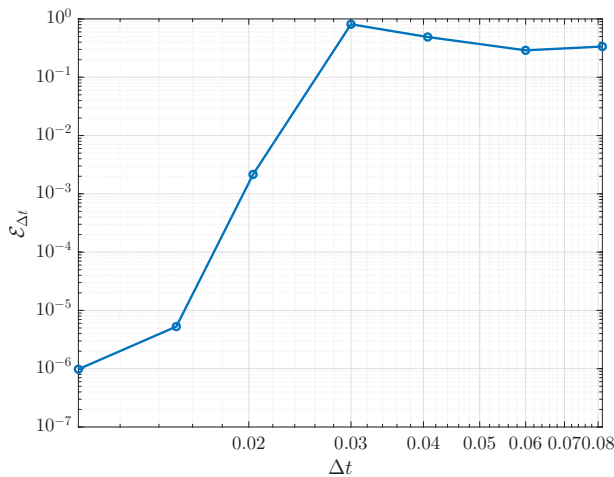


Figure 3: Convergence of the maximum error at $t = 6$, estimated on a grid, for the eight-source test of Section 6.1.

where the peak times are $t_{0,j} = 2 + 5j/M$, and inverse root widths $\mu_j = 30 + 20j/M$. Thus the peak times lie in $[2, 7]$ and the inverse root widths in $[30, 50]$. The largest inverse root width $\mu = 50$ is used to estimate K_0 as the frequency at which the Gaussian has dropped from each peak to ϵ , which gives $K_0 \approx 2\sqrt{\mu \log(10/\epsilon)} \approx 57$. We set the Nyquist fraction for the blending $\gamma = 2/3$; the blending region width (31) is $W = 14$ time steps.

We choose source points to be distributed on panels discretizing a “crueller” surface with the parametrization

$$\begin{aligned} \mathbf{x}(\theta, \psi) &= [(r_2 + H(\theta, \psi) \cos \psi) \cos \theta, (r_2 + H(\theta, \psi) \cos \psi) \sin \theta, H(\theta, \psi) \sin \psi], \\ H(\theta, \psi) &= r_1 + 0.1 \cos(5\theta + 3\psi), \quad \theta \in [0, 2\pi], \psi \in [0, 2\pi], \end{aligned}$$

where $r_1 = 0.3$ and $r_2 = 0.6$. This surface and its discretization is a variant of one used as a test case in [8], with different radius parameters chosen to just fit in the cube B .

We approximate the solution at the source points themselves using TK-WFP, over 326 time slices up to a final time $T = 6$, with the solution time interval $0 < t < T$ requiring $N_t = 326$ time steps with $\Delta t = 0.0184$. For this Δt , the truncation frequency was $K = 171$, needing $N = 313$ frequency modes per dimension at $\Delta k = 1.0962$. The typical number of targets within distance $\delta = 0.2577$ of each source is $M_{\text{typ}} = 917$. Recall that when evaluating the potential at the sources themselves, the self-interaction is excluded.

Comparing against the direct computation of u via (6), we find the relative maximum error to be $\tilde{\mathcal{E}}_{\Delta t} = 1.8 \times 10^{-5}$. Figure 4(a) shows the computed solution on the crueller at the final time, while the table in Figure 4(b) highlights the computational performance of TK-WFP compared to the direct evaluation

of u using (6). This test is carried out on a single Rome node with two 64-core AMD EPYC 7742 2.25 GHz CPUs (released 2019) and 1000 GB RAM. One sees from the table that the TK-WFP method is about 20 times faster than the naive evaluation of u .

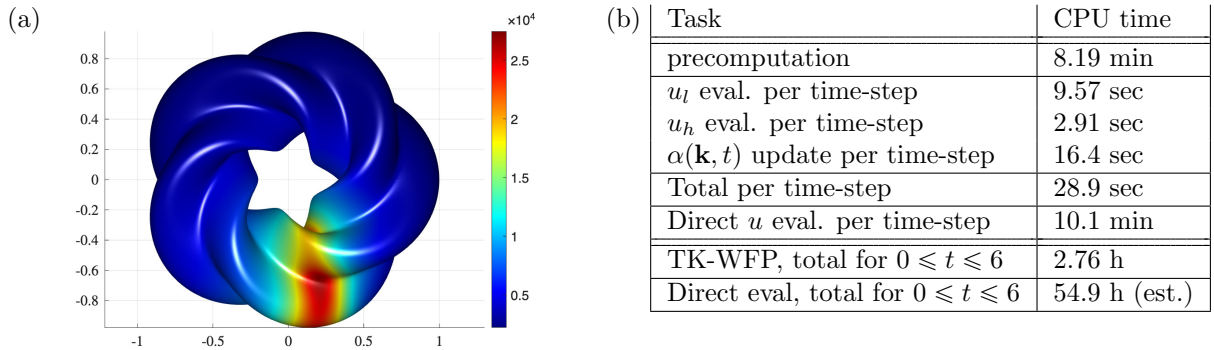


Figure 4: Results from the surface source and target distribution test of Section 6.2. Left: computed solution at $t = 6$ at the $M = 102400$ surface points, shown looking down the z -axis onto the xy -plane. Color indicates value of u , as per the colorscale shown. Right: CPU timing table for this experiment. Entries labeled with “est.” are estimated by scaling up from the cost for a single time-step.

6.3. Randomly located sources

We demonstrate the TK-WFP algorithm’s ability to handle a large number of sources and targets, in a range of low-to-high frequency settings. Specifically, we test TK-WFP with a million sources and targets, radiating the full range of center frequencies up to 30π where the computational box B has 30 wavelengths on a side. Given $M = 10^6$ sources placed at random locations within the box $[-1, 1]^3$, also imposing a 10^{-6} minimal distance between any two sources, we choose their time signatures

$$\sigma_j(t) = 0.5 [\text{erf}(5(t - t_{0,j})) + 1] \sin(\omega_j(t - t_{0,j})), \quad j = 1, \dots, M. \quad (45)$$

The starting times $t_{0,j}$ and frequencies ω_j are randomly selected from a set of M equidistant points in $t_{0,j} \in [1.5, 5]$ and $\omega_j \in [0, 30\pi]$. Because the maximum frequency and the smooth erf modulation widths are the same as in Section 6.1, the ϵ -bandlimit has the same value $K_0 \approx 131$. At this bandlimit the cube B has a side length about 42 wavelengths. We choose $\gamma = 0.5$ for the Nyquist blending fraction.

We evaluate the solution up to a final time $T = 6$ over a 100^3 uniform mesh of target points covering B , and 6 time slices in $[0, T]$. For the history evolution we use the time step $\Delta t = 0.012$ and $N_t = 502$. For the chosen Δt , $\delta = 0.2151$, and the typical number of neighboring sources to each target is $M_{\text{typ}} = 5214$. The solve requires a maximum frequency cut-off $K = 263$, $N = 477$ frequency modes, and $\Delta k = 1.105$.

Figure 5 presents the computed solution at $t = 4, 6$, while Figure 6(a) shows a slice at $t = 6$. The max-norm of the relative error over all space target points at the final time is $\tilde{\mathcal{E}}_{\Delta t} = 1.4 \times 10^{-6}$.

The timing table is shown in Figure 6(b), giving a breakdown of the computational performance of TK-WFP compared against the naive direct evaluation of (6). For the solve over all N_t steps, we observe an estimated factor of 75 speedup when using TK-WFP over the naive computation. For this test, a Cascade Lake node with four 24-core Xeon Platinum 8268 2.9 GHz CPUs (released 2019), and 2930 GB RAM, was used. We estimated that the maximum RAM usage of the code was under 500 GB.

7. Conclusion and discussion

We have presented the Truncated-Kernel Windowed Fourier Projection (TK-WFP) algorithm for the fast, high-order accurate evaluation of 3D hyperbolic potentials in free space. The method uses a smooth partition of unity (blending function) to split the potential into a local part involving only small separations, plus a smooth remainder (the “history” part) which can be approximated with spectral accuracy by a truncated Fourier integral. The method limits the history part’s rate of oscillation in frequency space via a smooth spatial truncation of the free-space 3D wave kernel beyond the diameter of the domain; this exploits strong Huygens and allows error-free Fourier discretization. The full history

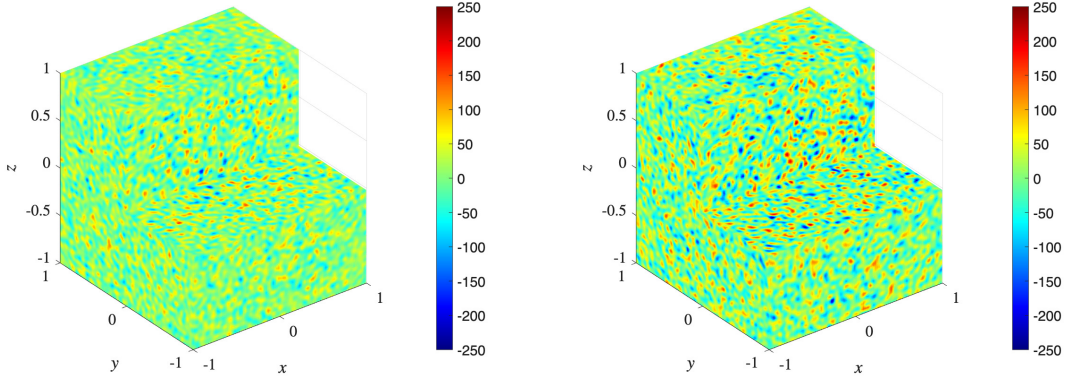


Figure 5: Computed solution at $t = 4$ (left) and $t = 6$ (right), for the test of Section 6.3 with 10^6 sources and targets. The solution is shown on a target grid of size 100^3 . There are 30 wavelengths per side of cube at the maximum center frequency of the sources, and about 42 wavelengths per side at the ϵ -bandlimit frequency. The relative maximum error at $t = 6$ is $\tilde{\mathcal{E}}_{\Delta t} = 1.4 \times 10^{-6}$.

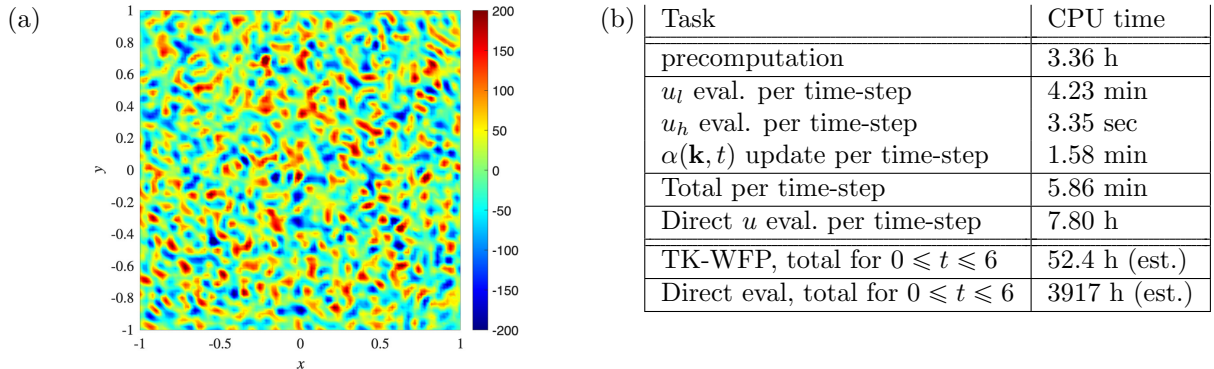


Figure 6: Results from the test of Section 6.3 with 10^6 sources and targets. Left: computed solution at the final time $t = 6$ on the slice $z = -0.01$. Right: CPU timing table for the experiment. Entries labeled with “est.” are estimated by scaling up from the cost for a single time-step.

dependence is compressed by exploiting a Duhamel-type update formula for each Fourier coefficient; the driving terms in this formula only involve the two narrow time intervals where the partition of unity is changing (creation and annihilation, as in Remark 4.1). This reduces the cost of evaluation from one that is quadratic with respect to the number of spatial and temporal points to one whose cost involves a linear term in the number of sources, plus a quasilinear term in the number of Fourier modes. Although the latter term does not result in the optimal scaling in the case of surface distributions, the scheme has a small prefactor and, being a two-level scheme, is much simpler to implement than hierarchical time-domain FMMs. (This is also true of the two-level FFT scheme of [5].)

We included a theoretical result that the Fourier truncation error drops exponentially with respect to the additional bandlimit introduced by the blending, when a Kaiser–Bessel function is used. We demonstrated the accuracy and efficiency of the scheme through three numerical examples, including one with a million sources and targets spanning more than 30 wavelengths per side of the computational domain.

The TK-WFP method can serve as an acceleration tool for the evaluation step in a variety of time-domain 3D wave-scattering scenarios: a large number of point-like (s-wave) scatterers, line-like scatterers (eg conductors using a slender-body approximation), surface boundary conditions, or a volumetric variable medium. In particular, our future plans include coupling the scheme with an integral representation, high-order surface quadratures, and a Volterra time marching scheme, to accelerate the method of [8].

Remark 7.1 (Periodic case and FFT size ratio). *If a periodic boundary condition is needed instead of the free space condition presented in this paper, two changes are needed: i) using G instead of the truncated kernel \mathcal{G}_A , and ii) fixing $\Delta k = \pi$ to give a Fourier series on $[-1, 1]^3$. We see that the ratio*

of (26) to this Δk is $A/2 + 1 \approx \sqrt{3} + 1$ (when $\delta \ll 1$), meaning that the NUFFT coefficient arrays (and hence FFTs) are $(\sqrt{3} + 1)^3 \approx 20$ times larger for TK-WFP than periodic WFP, all other things being equal. This ratio does not directly impact the method cost, because of rebalancing of local vs history parts. However, it does motivate further work on spectrally-accurate radiative conditions. Note that for interior wave problems (e.g. room acoustics), periodic conditions on an enclosing box are sufficient.

Remark 7.2 (Connection to prolate-based Ewald methods). The 3D WFP split of (12a)–(12b) may be viewed as a hyperbolic version of the Ewald split for 3D elliptic PDE (Poisson equation for periodic electrostatics); the latter traditionally uses Gaussians or, recently, prolates (see [49] and references within). The Kaiser–Bessel window ϕ' in WFP is a very close approximation to the prolate function used in [49], and in both methods the antiderivative is taken to get the blending function. However, in [49] only one half of the domain of the antiderivative is used, making the cutoff radius (analogous to δ) half the size of δ used in WFP for the same spectral bandlimit. It would be interesting to explore if *i*) WFP could be modified in the same way to reduce the cost of the local evaluation by a factor of 8, and *ii*) if the upsampling, currently implicit in the NUFFTs for WFP, can be avoided as in the 5-step particle mesh Ewald procedure.

Acknowledgements

We are grateful for discussions with Tom Hagstrom. The Flatiron Institute is a division of the Simons Foundation.

Appendix A. Proof of Lemma 2.1 on the decay of the Fourier transform of the window function

Starting from the Fourier transform of the Kaiser-Bessel window derivative ϕ' in (19), we have

$$\left| \hat{\phi}'(\omega) \right| \leq \frac{b}{\sinh b} \frac{1}{\sqrt{\left(\frac{\delta\omega}{2}\right)^2 - b^2}}, \quad |\omega| \geq \frac{2b}{\delta}, \quad (\text{A.1})$$

since the sinc is bounded by 1. Noting that $\sinh b = (1 - \epsilon^2)/2\epsilon < 1/2\epsilon$, for $0 < \epsilon < 1$, we get

$$\left| \hat{\phi}'(\omega) \right| < \frac{4\epsilon b}{\delta |\omega|} \frac{1}{\sqrt{1 - \left(\frac{2b}{\delta\omega}\right)^2}}, \quad |\omega| \geq \frac{2b}{\delta}. \quad (\text{A.2})$$

For $\theta > 1$, rearranging the inequality $|\omega| \geq 2b/\delta\sqrt{1 - 1/\theta^2}$ gives $1/\sqrt{1 - \left(\frac{2b}{\delta\omega}\right)^2} \leq \theta$, and (20) follows. \square

Appendix B. Proof of Theorem 1 on the decay of Fourier coefficients

We first establish the following Lemma on the Fourier transform of the pointwise product of two general functions whose Fourier transform satisfies decay properties for large frequencies.

Lemma B.1. *Let $f, g \in L^2(\mathbb{R})$, $h(t) = f(t)g(t)$, $t \in \mathbb{R}$, and $0 < \epsilon < 1$. Let \hat{f} , \hat{g} , and \hat{h} be the Fourier transforms of f, g and h respectively, as per the definition*

$$\hat{f}(\omega) = \int_{\mathbb{R}} e^{i\omega t} f(t) dt.$$

Suppose there exists C_1 and K_1 , and C_2 and K_2 , such that

$$\left| \hat{f}(\omega) \right| \leq \frac{C_1 \epsilon}{\omega^2}, \quad \text{for } |\omega| \geq K_1, \quad \text{and} \quad \left| \hat{g}(\omega) \right| \leq \frac{C_2 \epsilon}{\omega^2}, \quad \text{for } |\omega| \geq K_2. \quad (\text{B.1})$$

Then

$$\left| \hat{h}(\omega) \right| < \tilde{C} \frac{\epsilon}{\omega^2}, \quad \text{for } |\omega| \geq K_1 + K_2, \quad (\text{B.2})$$

where

$$\tilde{C} = \frac{1}{2\pi} \left[C_2 \|\hat{f}\|_1 \left(1 + \frac{K_1}{K_2}\right)^2 + C_1 \|\hat{g}\|_1 \left(1 + \frac{K_2}{K_1}\right)^2 + 8C_1 C_2 \left(\frac{1}{K_1} + \frac{1}{K_2}\right) \right].$$

Proof. By the convolution theorem

$$\hat{h}(\omega) = \frac{1}{2\pi} (\hat{f} * \hat{g})(\omega) = \frac{1}{2\pi} \int_{\mathbb{R}} \hat{f}(\xi) \hat{g}(\omega - \xi) d\xi. \quad (\text{B.3})$$

Fix $|\omega| \geq K_1 + K_2$, and consider partitioning $\hat{h}(\omega)$ into

$$\hat{h}(\omega) = \frac{1}{2\pi} (H_1(\omega) + H_2(\omega) + H_3(\omega)), \quad (\text{B.4})$$

where

$$H_l(\omega) := \int_{R_l(\xi)} \hat{f}(\xi) \hat{g}(\omega - \xi) d\xi, \quad l = 1, 2, 3, \quad (\text{B.5})$$

and

$$\begin{aligned} R_1(\xi) &:= \{\xi \in \mathbb{R} : |\xi| \leq K_1\}, \\ R_2(\xi) &:= \{\xi \in \mathbb{R} : |\xi| > K_1, |\omega - \xi| \geq K_2\}, \\ R_3(\xi) &:= \{\xi \in \mathbb{R} : |\xi| > K_1, |\omega - \xi| < K_2\}. \end{aligned} \quad (\text{B.6})$$

We seek upper bounds on each of H_l , $l = 1, 2, 3$.

In $R_1(\xi)$, and for $|\omega| \geq K_1 + K_2$, $|\omega - \xi| \geq |\omega| - |\xi| \geq |\omega| - K_1 \geq K_2$, then

$$|H_1(\omega)| \leq \int_{R_1(\xi)} |\hat{f}(\xi)| |\hat{g}(\omega - \xi)| d\xi \leq \int_{R_1(\xi)} \frac{C_2 \epsilon |\hat{f}(\xi)|}{|\omega - \xi|^2} d\xi \leq \frac{C_2 \epsilon}{(|\omega| - K_1)^2} \|\hat{f}\|_1. \quad (\text{B.7})$$

Similarly, using a change of variables, we have

$$|H_3(\omega)| \leq \int_{R_3(\omega - \eta)} |\hat{f}(\omega - \eta)| |\hat{g}(\eta)| d\eta \leq \frac{C_1 \epsilon}{(|\omega| - K_2)^2} \|\hat{g}\|_1. \quad (\text{B.8})$$

Finally consider

$$|H_2(\omega)| \leq \int_{R_2(\xi)} |\hat{f}(\xi)| |\hat{g}(\omega - \xi)| d\xi \leq C_1 C_2 \epsilon^2 \int_{R_2(\xi)} \frac{1}{\xi^2 (\omega - \xi)^2} d\xi, \quad (\text{B.9})$$

and split R_2 further into

$$\begin{aligned} R_{2,1}(\xi) &:= \{\xi \in \mathbb{R} : |\xi| > K_1, |\omega - \xi| > K_2, |\xi| \leq |\omega|/2\}, \\ R_{2,2}(\xi) &:= \{\xi \in \mathbb{R} : |\xi| > K_1, |\omega - \xi| > K_2, |\xi| > |\omega|/2\}. \end{aligned} \quad (\text{B.10})$$

In $R_{2,1}$, $|\omega - \xi| \geq |\omega| - |\xi| \geq |\omega|/2$ so that

$$\int_{R_{2,1}(\xi)} \frac{1}{\xi^2 (\omega - \xi)^2} d\xi \leq \frac{4}{\omega^2} \int_{R_{2,1}(\xi)} \frac{1}{\xi^2} d\xi \leq \frac{8}{K_1 \omega^2}. \quad (\text{B.11})$$

Similarly in $R_{2,2}$, a change of variables gives

$$\int_{R_{2,2}(\xi)} \frac{1}{\xi^2 (\omega - \xi)^2} d\xi = \int_{R_{2,2}(\omega - \eta)} \frac{1}{\eta^2 (\omega - \eta)^2} d\eta \leq \frac{8}{K_2 \omega^2}. \quad (\text{B.12})$$

Hence,

$$|H_2(\omega)| \leq \frac{8C_1 C_2 \epsilon^2}{\omega^2} \left(\frac{1}{K_1} + \frac{1}{K_2} \right). \quad (\text{B.13})$$

Therefore,

$$\left| \hat{h}(\omega) \right| \leq \frac{1}{2\pi} \left[\frac{C_2 \|\hat{f}\|_1}{(|\omega| - K_1)^2} \epsilon + \frac{8C_1 C_2}{\omega^2} \left(\frac{1}{K_1} + \frac{1}{K_2} \right) \epsilon^2 + \frac{C_1 \|\hat{g}\|_1}{(|\omega| - K_2)^2} \epsilon \right]. \quad (\text{B.14})$$

Note that $|\omega| - K_1 > \frac{K_2}{K_1 + K_2} |\omega|$, whenever $|\omega| > K_1 + K_2$, and similarly $|\omega| - K_2 > \frac{K_1}{K_1 + K_2} |\omega|$, then

$$\left| \hat{h}(\omega) \right| \leq \frac{1}{2\pi} \frac{1}{\omega^2} \left[C_2 \|\hat{f}\|_1 \left(1 + \frac{K_1}{K_2} \right)^2 \epsilon + C_1 \|\hat{g}\|_1 \left(1 + \frac{K_2}{K_1} \right)^2 \epsilon + 8C_1 C_2 \left(\frac{1}{K_1} + \frac{1}{K_2} \right) \epsilon^2 \right]. \quad (\text{B.15})$$

Noting that $\epsilon^2 < \epsilon$ completes the proof. \square

Remark B.1. If $f \in L^2(\mathbb{R})$ such that $|\hat{f}(\omega)| \leq C_1 \epsilon \omega^{-2}$, for $|\omega| \geq K_1$, then $\|\hat{f}\|_1 < \infty$ because

$$\|\hat{f}\|_1 = \int_{|\omega| < K_1} |\hat{f}(\omega)| d\omega + \int_{|\omega| > K_1} |\hat{f}(\omega)| d\omega \leq \sqrt{2K_1} \|\hat{f}\|_2 + \frac{2C_1 \epsilon}{K_1} < \infty, \quad (\text{B.16})$$

using Cauchy-Schwarz inequality and the decay of \hat{f} .

We now prove Theorem 1. The vanishing properties of ϕ allow the extension of the integration limits in the definition of $\alpha(\mathbf{k}, t)$ in (24) to the real line, so that

$$\alpha(\mathbf{k}, t) = \int_{\mathbb{R}} \frac{\sin \kappa(t - \tau)}{\kappa} S(\mathbf{k}, \tau) \phi(t - \tau) \phi(A - t + \tau) d\tau. \quad (\text{B.17})$$

Define

$$\chi(\mathbf{k}, t; \tau) := S(\mathbf{k}, \tau) \psi(t - \tau),$$

where

$$\psi(\tau) := \phi(\tau) \phi(A - \tau) = \phi(\tau) [1 - \phi(\tau - A + \delta)] = \phi(\tau) - \phi(\tau - A + \delta), \quad (\text{B.18})$$

where we exploited the inversion symmetry $\phi(\delta - \tau) = 1 - \phi(\tau)$ and other properties of ϕ . We find that for $t \in [0, T]$,

$$\psi(\tau) = \int_{\tau - A + \delta}^{\tau} \phi'(s) ds, \quad \text{and} \quad \hat{\psi}(\omega) = \frac{\hat{\phi}'(\omega)}{i\omega} \left(e^{i\omega(A - \delta)} - 1 \right). \quad (\text{B.19})$$

Therefore, by Lemma 2.1, and for some $\theta > 1$, we have

$$\left| \hat{\psi}(\omega) \right| \leq \frac{2 \left| \hat{\phi}'(\omega) \right|}{|\omega|} < \frac{4b\theta}{\delta} \cdot \frac{\epsilon}{\omega^2}, \quad \text{whenever} \quad |\omega| \geq \frac{2b}{\delta \sqrt{1 - \theta^{-2}}}. \quad (\text{B.20})$$

Furthermore, for fixed \mathbf{k} and t , the function $\chi(\mathbf{k}, t; \tau)$ is $L^2(\mathbb{R})$ with respect to τ , and is a product of $S(\mathbf{k}, t)$ and $\psi(t - \tau)$, whose Fourier transforms with respect to τ satisfy the following decay properties

$$\left| \hat{S}(\mathbf{k}, \omega) \right| \leq M \cdot \frac{\epsilon}{\omega^2}, \quad |\omega| \geq K_0, \quad \text{and} \quad \left| \hat{\psi}(\omega) \right| < \frac{4b\theta}{\delta} \cdot \frac{\epsilon}{\omega^2}, \quad |\omega| \geq K_1, \quad (\text{B.21})$$

where $K_1 := 2b/\delta\sqrt{1 - \theta^{-2}}$. Then by Lemma B.1, the Fourier transform of χ with respect to τ , denoted by $\hat{\chi}(\mathbf{k}, t; \omega)$, satisfies the property

$$\left| \hat{\chi}(\mathbf{k}, t; \omega) \right| < c_1 \frac{\epsilon}{\omega^2}, \quad \text{for} \quad |\omega| > K, \quad (\text{B.22})$$

where $K = K_0 + K_1$ is the total bandlimit as stated in (28) in the theorem, and

$$c_1 = \frac{1}{2\pi} \left[\frac{4b\theta}{\delta} \left(\sum_{j=1}^M \|\hat{\sigma}_j\|_1 \right) \left(1 + \frac{K_0}{K_1} \right)^2 + M \|\hat{\psi}\|_1 \left(1 + \frac{K_1}{K_0} \right)^2 + 8 \cdot \frac{4b\theta}{\delta} M \left(\frac{1}{K_0} + \frac{1}{K_1} \right) \right].$$

With the following upper bounds on $\|\hat{\sigma}_j\|_1$ and $\|\hat{\psi}\|_1$,

$$\|\hat{\sigma}_j\|_1 \leq 2K_0\|\sigma_j\|_1 + \frac{2\epsilon}{K_0}, \quad \|\hat{\psi}\|_1 \leq 2K_1A + \frac{4b\theta}{\delta} \cdot \frac{2\epsilon}{K_1}, \quad (\text{B.23})$$

and the property that $\|\sigma_j\|_1 \leq P$ for all $j = 1, \dots, M$, we have

$$c_1 \leq \frac{1}{2\pi} \left[\frac{8b\theta M}{\delta} \left(K_0P + \frac{1}{K_0} \right) \left(\frac{K}{K_1} \right)^2 + 2M \left(K_1A + \frac{4b\theta}{\delta K_1} \right) \left(\frac{K}{K_0} \right)^2 + 8 \cdot \frac{4b\theta M}{\delta} \left(\frac{K}{K_0K_1} \right) \right]. \quad (\text{B.24})$$

Plugging the expression of K_1 , noting that $\sqrt{1-\theta^{-2}} < 1$, and simplifying gives

$$c_1 < CM, \quad \text{where } C := \frac{K}{\pi K_0 \sqrt{1-\theta^{-2}}} \left\{ \frac{2AbK}{\delta K_0} + (\theta - \theta^{-1}) \left[\frac{\delta K}{b} (K_0^2 P + 1) + \frac{2K}{K_0} + 8 \right] \right\}. \quad (\text{B.25})$$

We use Equation (B.22) and the inequality in (B.25) to establish the decay property on $\alpha(\mathbf{k}, t)$ given in (28). Writing $\sin \kappa(t - \tau)$ in terms of complex exponentials gives

$$\begin{aligned} t\alpha(\mathbf{k}, t) &= \frac{1}{2i\kappa} \left[e^{i\kappa t} \int_{\mathbb{R}} e^{-i\kappa\tau} \chi(\mathbf{k}, t; \tau) d\tau - e^{-i\kappa t} \int_{\mathbb{R}} e^{i\kappa\tau} \chi(\mathbf{k}, t; \tau) d\tau \right], \\ &= \frac{1}{2i\kappa} \left[e^{i\kappa t} \hat{\chi}(\mathbf{k}, t; -\kappa) - e^{-i\kappa t} \hat{\chi}(\mathbf{k}, t; \kappa) \right], \end{aligned} \quad (\text{B.26})$$

so that

$$|\alpha(\mathbf{k}, t)| \leq \frac{1}{2\kappa} (|\hat{\chi}(\mathbf{k}, t; -\kappa)| + |\hat{\chi}(\mathbf{k}, t; \kappa)|). \quad (\text{B.27})$$

Finally, applying Equation (B.22) and (B.24) yields the claimed inequality (28), with the constant C as in (B.25). As claimed, (B.25) shows that C grows weakly with respect to the parameters (at most quadratic with respect to bandlimit, when considering combined powers of K_0 , K , and b/δ , and linear in all other parameters). \square

References

- [1] R. Guenther, J. Lee, *Partial Differential Equations of Mathematical Physics and Integral Equations*, Dover Books on Mathematics, Dover Publications, 2012.
- [2] M. Costabel, Time-dependent problems with the boundary integral equation method, in: E. Stein, R. de Borst, T. Hughes (Eds.), *Encyclopedia of Computational Mechanics*, Vol. 2, part II, John Wiley & Sons, Ltd., 2004, p. 943.
- [3] F.-J. Sayas, Retarded potentials and time domain boundary integral equations: a road map, *Springer Series in Computational Mathematics*, 50, Springer, 2016.
- [4] D. Colton, R. Kress, *Integral equation methods in scattering theory*, Wiley, 1983.
- [5] A. Yilmaz, J.-M. Jin, E. Michielssen, Time domain adaptive integral method for surface integral equations, *IEEE Trans. Antennas Propag.* 52 (10) (2004) 2692–2708. doi:10.1109/TAP.2004.834399.
- [6] L. Banjai, M. Kachanovska, Fast convolution quadrature for the wave equation in three dimensions, *J. Comput. Phys.* 279 (2014) 103–126. doi:10.1016/j.jcp.2014.08.049.
- [7] F.-J. Sayas, *Retarded Potentials and Time-Domain Boundary Integral Equation*, Springer, 2016.
- [8] A. Barnett, L. Greengard, T. Hagstrom, High-order discretization of a stable time-domain integral equation for 3D acoustic scattering, *J. Comput. Phys.* 402 (2020) 109047. doi:https://doi.org/10.1016/j.jcp.2019.109047.
- [9] Y. Liu, E. Michielssen, Parallel fast time-domain integral-equation methods for transient electromagnetic analysis, in: A. Grama, A. H. Sameh (Eds.), *Parallel Algorithms in Computational Science and Engineering*, Springer International Publishing, Cham, 2020, pp. 347–379. doi:10.1007/978-3-030-43736-7_12.
- [10] M. Kaltenbacher, *Computational acoustics*, Springer, 2018.
- [11] H. Wang, I. Sihar, R. P. Muñoz, M. Hornikx, Room acoustics modelling in the time-domain with the nodal discontinuous Galerkin method, *J. Acoust. Soc. Am.* 145 (4) (2019) 2650. doi:10.1121/1.5096154.
- [12] W. C. Chew, *Waves and Fields in Inhomogeneous Media*, Wiley-IEEE Press, 1999.
- [13] W. C. Chew, J. M. Jin, E. Michielssen, J. Song, *Fast and Efficient Algorithms in Computational Electromagnetics*, Artech House, Boston, MA, 2001.
- [14] J. Virieux, V. Etienne, V. Cruz-Atienza, R. Brossier, E. Chaljub, O. Coutant, S. Garambois, D. Mercierat, V. Prieux, S. Operto, A. Ribodetti, J. Tago, Modelling seismic wave propagation for geophysical imaging, in: M. Kanao (Ed.), *Seismic Waves - Research and Analysis*, IntechOpen, London, 2012, Ch. 13, pp. 253–304. doi:10.5772/30219.
- [15] N. G. Al Hassanieh, A. H. Barnett, L. Greengard, A fast algorithm for the wave equation using time-windowed Fourier projection (2025). arXiv:2507.07823.
- [16] F. Vico, L. Greengard, M. Ferrando, Fast convolution with free-space Green's functions, *J. Comput. Phys.* 323 (2016) 191–203. doi:10.1016/j.jcp.2016.07.028.

- [17] A. Ergin, B. Shanker, E. Michielssen, Fast evaluation of three-dimensional transient wave fields using diagonal translation operators, *J. Comput. Phys.* 146 (1) (1998) 157–180. doi:10.1006/jcph.1998.5908.
- [18] J. Meng, A. Boag, V. Lomakin, E. Michielssen, A multilevel Cartesian non-uniform grid time domain algorithm, *J. Comput. Phys.* 229 (22) (2010) 8430–8444. doi:10.1016/j.jcp.2010.07.026.
- [19] T. G. Anderson, O. P. Bruno, M. Lyon, High-order, dispersionless “fast-hybrid” wave equation solver. Part I: $O(1)$ sampling cost via incident-field windowing and recentering, *SIAM J. Sci. Comput.* 42 (2) (2020) A1348–A1379. doi:10.1137/19m1251953.
- [20] O. P. Bruno, M. A. Santana, Efficient time-domain scattering synthesis via frequency-domain singularity subtraction (2025). arXiv:2505.06189.
- [21] H. Wilber, W. Vaes, A. Gopal, G. Martinsson, A time-frequency method for acoustic scattering with trapping (2025). arXiv:2506.15165.
- [22] J. S. Hesthaven, T. Warburton, Nodal discontinuous Galerkin methods — Algorithms, analysis, and applications, Springer, New York, 2008.
- [23] B. Engquist, A. Majda, Absorbing boundary conditions for numerical simulation of waves, *Proc. Nat. Acad. Sci.* 74 (5) (1977) 1765–1766. doi:10.1073/pnas.74.5.1765.
- [24] A. Bayliss, E. Turkel, Radiation boundary conditions for wave-like equations, *Comm. Pure Appl. Math.* 33 (6) (1980) 707–725. doi:10.1002/cpa.3160330603.
- [25] R. L. Higdon, Radiation boundary conditions for elastic wave propagation, *SIAM J. Numer. Anal.* 27 (4) (1990) 831–869. doi:10.1137/0727049.
- [26] M. Israeli, S. A. Orszag, Approximation of radiation boundary conditions, *J. Comput. Phys.* 41 (1) (1981) 115–135. doi:10.1016/0021-9991(81)90082-6.
- [27] J.-P. Berenger, A perfectly matched layer for the absorption of electromagnetic waves, *J. Comput. Phys.* 114 (2) (1994) 185–200. doi:10.1006/jcph.1994.1159.
- [28] D. Givoli, Computational absorbing boundaries, in: S. Marburg, B. Nolte (Eds.), *Computational Acoustics of Noise Propagation in Fluids - Finite and Boundary Element Methods*, Springer Berlin Heidelberg, Berlin, Heidelberg, 2008, Ch. 5, pp. 145–166. doi:10.1007/978-3-540-77448-8_6.
- [29] T. Hagstrom, Radiation boundary conditions for the numerical simulation of waves, *Acta Numer.* 8 (1999) 47–106. doi:10.1017/S0962492900002890.
- [30] S. V. Tsynkov, Numerical solution of problems on unbounded domains, *Appl. Numer. Math.* 27 (1998) 465–532.
- [31] A. Zenginoğlu, Hyperboloidal layers for hyperbolic equations on unbounded domains, *J. Comput. Phys.* 230 (6) (2011) 2286–2302. doi:10.1016/j.jcp.2010.12.016.
- [32] A. Kahana, F. Smith, E. Turkel, S. Tsynkov, A high order compact time/space finite difference scheme for the 2D and 3D wave equation with a damping layer, *J. Comput. Phys.* 460 (2022) 111161. doi:10.1016/j.jcp.2022.111161.
- [33] T. Hagstrom, T. Warburton, A new auxiliary variable formulation of high-order local radiation boundary conditions: corner compatibility conditions and extensions to first-order systems, *Wave Motion* 39 (4) (2004) 327–338, new computational methods for wave propagation. doi:10.1016/j.wavemoti.2003.12.007.
- [34] T. Hagstrom, T. Warburton, Complete radiation boundary conditions: Minimizing the long time error growth of local methods, *SIAM J. Numer. Anal.* 47 (5) (2009) 3678–3704. doi:10.1137/090745477.
- [35] T. Hagstrom, T. Warburton, D. Givoli, Radiation boundary conditions for time-dependent waves based on complete plane wave expansions, *J. Comput. Appl. Math.* 234 (6) (2010) 1988–1995, eighth International Conference on Mathematical and Numerical Aspects of Waves (Waves 2007). doi:10.1016/j.cam.2009.08.050.
- [36] T. Potter, J. Shrage, D. Lumley, Performance of the double absorbing boundary method when applied to the 3D acoustic wave equation, *ASEG Extended Abstracts 2015* (12 2015). doi:10.1071/ASEG2015ab010.
- [37] B. Alpert, L. Greengard, T. Hagstrom, Rapid evaluation of nonreflecting boundary kernels for time-domain wave propagation, *SIAM J. Numer. Anal.* 37 (4) (2000) 1138–1164. doi:10.1137/S0036142998336916.
- [38] M. J. Grote, J. B. Keller, Exact nonreflecting boundary conditions for the time dependent wave equation, *SIAM J. Appl. Math.* 55 (2) (1995) 280–297, perturbation methods in physical mathematics (Troy, NY, 1993).
- [39] V. S. Ryaben’kii, S. V. Tsynkov, V. I. Turchaninov, Global discrete artificial boundary conditions for time-dependent wave propagation, *J. Comput. Phys.* 174 (2001) 712–758.
- [40] A. Soffer, C. Stucchio, Open boundaries for the nonlinear Schrödinger equation, *J. Comput. Phys.* 225 (2) (2007) 1218–1232. doi:10.1016/j.jcp.2007.01.020.
- [41] C. Stucchio, A. Soffer, Multiscale resolution of shortwave-longwave interaction, *Comm. Pure Appl. Math.* 62 (1) (2009) 82–124.
- [42] A. Soffer, C. Stucchio, M.-B. Tran, *Time Dependent Phase Space Filters: A Stable Absorbing Boundary Condition*, Springer Briefs on PDEs and Data Science, Springer Nature, 2023.
- [43] A. Bayliss, C. Goldstein, E. Turkel, On accuracy conditions for the numerical computation of waves, *J. Comput. Phys.* 59 (1985) 396–404.
- [44] E. M. Stein, G. Weiss, *Introduction to Fourier Analysis on Euclidean Spaces (PMS-32)*, Princeton University Press, 1971.
- [45] L. N. Trefethen, J. A. C. Weideman, The exponentially convergent trapezoidal rule, *SIAM Rev.* 56 (3) (2014) 385–458. doi:10.1137/130932132.
- [46] A. H. Barnett, How exponentially ill-conditioned are contiguous submatrices of the Fourier matrix?, *SIAM Rev.* 64 (1) (2022). doi:10.1137/20M1336837.
- [47] A. H. Barnett, J. Magland, L. af Klinteberg, A parallel non-uniform fast Fourier transform library based on an “exponential of semicircle” kernel, *SIAM J. Sci. Comput.* 41 (2019) C479–C504.
- [48] A. H. Barnett, *et al.*, *Flatiron Institute Nonuniform Fast Fourier Transform* (2018–2025). URL <https://github.com/flatironinstitute/finufft>
- [49] J. Liang, L. Lu, A. Barnett, L. Greengard, S. Jiang, Accelerating fast Ewald summation with prolates for molecular dynamics simulations (2025). arXiv:2505.09727.